



Whistler Waves as a Signature of Converging Magnetic Holes in Space Plasmas

Wence Jiang^{1,2,3} , Daniel Verscharen³ , Hui Li^{1,2} , Chi Wang^{1,2} , and Kristopher G. Klein⁴ ¹ State Key Laboratory of Space Weather, National Space Science Center, CAS, Beijing, People's Republic of China; joe.jiang@ucl.ac.uk, hli@nssc.ac.cn, cw@spaceweather.ac.cn² University of Chinese Academy of Sciences, Beijing, People's Republic of China³ Mullard Space Science Laboratory, University College London, Dorking RH5 6NT, UK; d.verscharen@ucl.ac.uk⁴ Department of Planetary Sciences, University of Arizona, Tucson, AZ, USA; kglein@arizona.edu

Received 2022 May 17; revised 2022 June 23; accepted 2022 June 27; published 2022 August 24

Abstract

Magnetic holes are plasma structures that trap a large number of particles in a magnetic field that is weaker than the field in its surroundings. The unprecedented high time-resolution observations by NASA's Magnetospheric Multiscale Mission enable us to study the particle dynamics in magnetic holes in the Earth's magnetosheath in great detail. We reveal the local generation mechanism of whistler waves by a combination of Landau-resonant and cyclotron-resonant wave-particle interactions of electrons in response to the large-scale evolution of a magnetic hole. As the magnetic hole converges, a pair of counter-streaming electron beams form near the hole's center as a consequence of the combined action of betatron and Fermi effects. The beams trigger the generation of slightly oblique whistler waves. Our conceptual prediction is supported by a remarkable agreement between our observations and numerical predictions from the Arbitrary Linear Plasma Solver. Our study shows that wave-particle interactions are fundamental to the evolution of magnetic holes in space and astrophysical plasmas.

Unified Astronomy Thesaurus concepts: [Space plasmas \(1544\)](#); [Planetary magnetospheres \(997\)](#); [Solar wind \(1534\)](#); [Interplanetary turbulence \(830\)](#)

1. Introduction

Space and astrophysical plasmas exhibit electromagnetic fluctuations and inhomogeneous structures across a very broad range of scales (Schekochihin et al. 2009; Alexandrova et al. 2013; Verscharen et al. 2019b). In the Earth's magnetosheath, plasma turbulence and coherent structures are abundant as a consequence of the plasma's bow-shock crossing and processes around the magnetopause such as magnetic reconnection and field draping (Retinò et al. 2007; Tsurutani et al. 2011; Karimabadi et al. 2014).

Magnetic holes are an important type of spatially nonuniform and nonlinear coherent plasma structure. They are characterized by a local dip in the magnetic field with an anticorrelation between density and magnetic-field variations. They occur in the terrestrial magnetosheath (Tsurutani et al. 1982; Fazakerley & Southwood 1994; Cattaneo et al. 1998; Sahraoui et al. 2006; Yao et al. 2020) and other space plasmas like the solar wind (Tsurutani et al. 2011), the heliosheath (Burlaga et al. 2006), and cometary environments (Russell et al. 1987; Plaschke et al. 2018). A candidate mechanism for the creation of magnetic holes is the mirror-mode instability, which is a nonpropagating electromagnetic plasma instability (Chandrasekhar et al. 1958; Hasegawa 1969; Kaufmann et al. 1970; Tsurutani et al. 1982; Southwood & Kivelson 1993; Fazakerley & Southwood 1994; Fazakerley et al. 1995; Kuznetsov et al. 2007; Soucek et al. 2008; Kunz et al. 2014). Alternative generation mechanisms include solitons (Baumgärtel 1999; Li et al. 2016), phase-steepened Alfvén waves (Tsurutani et al. 2002), and decaying turbulence (Haynes et al. 2015).

The spatial scale of magnetic holes in the Earth's magnetosheath varies from $10\rho_e$ (≈ 10 km) to $5\text{--}40\rho_p$ ($\approx 500\text{--}3000$ km; Tsurutani et al. 2011; Liu et al. 2020; Yao et al. 2020), where ρ_e and ρ_p are the gyroradii of the electrons and protons. Magnetic holes are capable of trapping particles due to the mirror force from their nonuniform magnetic field. These trapped particles bounce back and forth between the mirror points of these structures. At small scales, kinetic effects such as microinstabilities can regulate the dynamics of both the trapped and the untrapped particles in magnetic holes via wave-particle interactions. If a magnetic hole changes in depth, betatron and type-1 Fermi acceleration cause the particles to evolve collectively in velocity space (Southwood & Kivelson 1993; Pantellini et al. 1995; Kivelson & Southwood 1996; Chisham et al. 1998; Soucek & Escoubet 2011; Ahmadi et al. 2018; Breuillard et al. 2018; Li et al. 2021). However, there is still a significant lack of direct evidence for particle diffusion in wave-particle interactions at kinetic scales and of the understanding of the multiscale evolution of magnetic holes. Here, we present such direct evidences for these processes and the important role of wave-particle interactions in a converging magnetic hole based on on multispacecraft data from the Magnetospheric Multiscale (MMS) mission.

2. Particle Diffusion in Converging Magnetic Holes: a Multiscale Model

In this section, we develop a conceptual model to explain the multiscale evolution of a converging magnetic hole. We summarize our model visually in Figure 1.

The magnetic hole is characterized by a spatially nonuniform magnetic-field configuration with a significant number of particles trapped near the magnetic-field minimum (illustrated as the purple shade in Figure 1(a)). Due to the nonuniform magnetic field associated with the magnetic hole, particles are subject to the mirror force when their magnetic moment is conserved. The

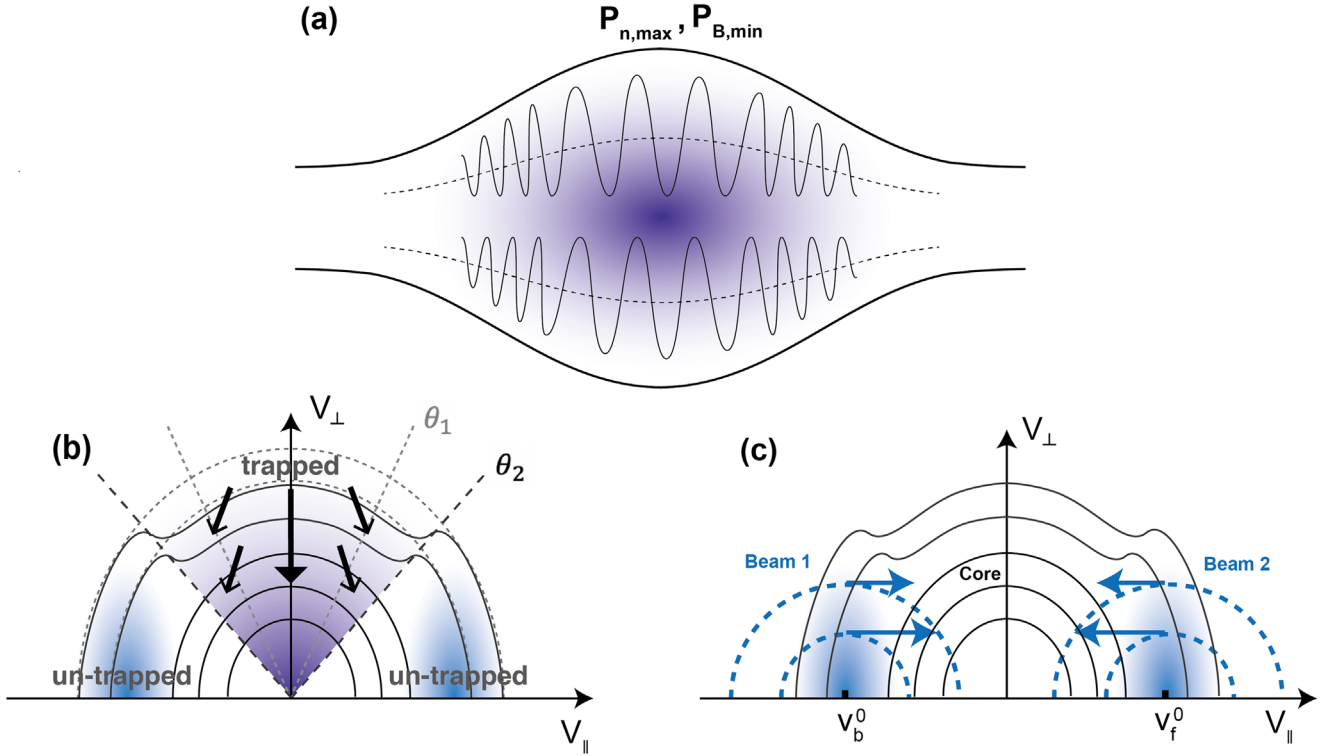


Figure 1. Illustration of our conceptual model for a converging magnetic hole. (a) A schematic of the trapped electrons (shaded) in a magnetic hole. The black spirals centered on the dotted lines represent the bouncing electron trajectories. (b) A sketch of the formation of beams in velocity space by Fermi acceleration and the betatron effect during the convergence of the magnetic hole. Particle velocity-space trajectories at different pitch angles are shown by the black arrows. (c) A sketch of quasi-linear diffusion paths in a two-beam electron velocity distribution function. The particle diffusion paths (blue arrows) are locally tangent to semicircles (shown in blue) about the parallel phase speeds $v_f^0 = \omega_w/|k_{||}$ of the forward-propagating waves and $v_b^0 = -\omega_w/|k_{||}$ of the backward-propagating waves. The diffusion paths always point toward lower phase space density. For (b) and (c), the electron distribution is shown as black semicircles and two beams are highlighted as blue shaded areas.

trapping of particles is described by a critical pitch-angle θ_c (Kivelson & Southwood 1996), so that

$$\sin \theta_c = \sqrt{B/B_{\max}}, \quad (1)$$

where B and B_{\max} are the local magnetic field and the maximum magnetic field of the structure. Particles with a pitch-angle θ that fulfills $\theta_c < \theta < (180^\circ - \theta_c)$ are effectively trapped and bounce between their mirror points where their velocity component parallel to the magnetic field reverses its sign. This particle motion with the overlaid gyration motion is illustrated by the black spirals in Figure 1(a). Particles with a pitch-angle $\theta < \theta_c$ and $\theta > (180^\circ - \theta_c)$ — inside the loss cone — stream through the magnetic hole. The trapping of particles marks the formation of a nonpropagating spatial structure by retaining pressure balance between the local magnetic pressure P_B and the local plasma thermal pressure P_n (Schwartz et al. 1996; Soucek & Escoubet 2011). If the magnetic hole is not in pressure balance (Yao et al. 2020), it either converges or diverges until pressure balance is achieved.

In a converging magnetic hole, the convergence of the mirror points of the trapped particles causes type-1 Fermi acceleration. The decreasing magnetic field in a converging magnetic hole causes betatron cooling of the particles (Southwood & Kivelson 1993) due to the conservation of the magnetic moment. The Fermi acceleration increases the velocity component of the trapped particles in the directions parallel and antiparallel to the magnetic field, while the betatron cooling decreases the velocity component of the trapped particles in the perpendicular direction.

Assuming gyrotropy, Figure 1(b) shows the isocontours of the velocity distribution function (VDF) $f_e(v_{||}, v_{\perp})$ of particles in the plasma frame in a magnetic hole, where $v_{||}$ and v_{\perp} are the velocity components parallel and perpendicular to the magnetic field. The dashed black and gray lines represent different critical pitch angles according to Equation (1) for different local magnetic fields, referred to as θ_{c1} or $180^\circ - \theta_{c1}$, and θ_{c2} or $180^\circ - \theta_{c2}$. Trapped particles are illustrated with a purple shade in Figure 1(b). The black arrows in Figure 1(b) show the velocity-space trajectories of particles with different pitch angles due to Fermi acceleration and betatron cooling as the magnetic hole converges.

As a consequence of the Fermi and betatron effects, a pair of counter-streaming electron beams (blue shaded in Figures 1(b)–(c)) form in velocity space. Beams represent a non-equilibrium plasma state that can drive kinetic microinstabilities (Gary 1993). In particular, counter-streaming electron beams can drive unstable electromagnetic whistler waves with right-handed polarization and frequencies below the local electron cyclotron frequency.

Whistler waves are frequently observed in magnetic holes, but the excitation and origin of these waves are a matter of ongoing research (Zhang et al. 1998; Huang et al. 2019; Ren et al. 2019; Yao et al. 2019; Kitamura et al. 2020). Recently, so-called pancake, donut-shaped, or butterfly pitch-angle distributions with beams of electrons have been proposed as sources for the wave excitation possibly via cyclotron resonances (Zhima et al. 2015; Ahmadi et al. 2018; Breuillard et al. 2018; Behar et al. 2020; Huang et al. 2020; Zhang et al. 2021). However, there is still a lack of consistent evidence underpinning the nature of the

resonant waves and the role of the quasi-linear evolution of these instabilities for the evolution of magnetic holes.

In quasi-linear theory, field-aligned electron beams evolve under the action of whistler-wave instabilities via either Landau or cyclotron-resonant wave–particle interactions (Shapiro & Shevchenko 1962; Kennel & Engelmann 1966; Rowlands et al. 1966; Verscharen et al. 2019a; Jeong et al. 2020). The particles that participate in resonant wave–particle interactions have a velocity component v_{\parallel} parallel to the local magnetic field that fulfills the resonance condition

$$v_{\parallel} = v_{\text{res}}^n = \frac{\omega_w + n\Omega_e}{k_{\parallel}}, \quad (2)$$

where v_{res}^n is the n th resonance speed, ω_w is the real part of the whistler-wave frequency, k_{\parallel} is the parallel wavenumber, n is an integer, $\Omega_e = eB/m_e$ is the electron gyrofrequency, e is the electron charge, B is the magnetic field, and m_e is the electron mass. The Landau resonance condition corresponds to $n=0$ in Equation (2). In that case, only electrons with $v_{\parallel} = v_{\text{res}}^0 = \omega_w/k_{\parallel}$ resonate and secularly exchange energy with the waves. Meanwhile, resonant electrons undergo diffusion in velocity space along specific trajectories.

Using a similar format as Figure 1(b), we illustrate the Landau-resonant interaction between counter-streaming electron beams and unstable whistler waves in Figure 1(c). In these interactions, electrons transfer energy to the waves and thus drive them unstable only if they lose energy when undergoing quasi-linear diffusion. Since velocity-space diffusion always occurs from larger values of f_e to smaller values of f_e , this condition requires that $\partial f_e/\partial v_{\parallel} > 0$ at v_{f}^0 (i.e., forward-propagating waves), and $\partial f_e/\partial v_{\parallel} < 0$ at v_{b}^0 (i.e., backward-propagating waves). Unstable slightly oblique whistler waves with $k_{\parallel} > 0$ and $k_{\perp} < 0$ are excited, and the parallel/antiparallel component of the wave electric field is responsible for the particle diffusion.

In Figure 1(c), blue dashed semicircles illustrate the diffusion paths of resonant particles that undergo wave–particle interactions. The direction of the diffusion is always tangent to semicircles around the associated ω_w/k_{\parallel} since quasi-linear diffusion is energy-conserving in the reference frame that moves with the parallel phase speed of the resonant waves (Verscharen et al. 2019b). We use blue arrows in Figure 1(c) to illustrate the diffusion trajectories of Landau-resonant electrons in our case.

For consistency, our multiscale model requires that the quasi-linear diffusion rate ν_d is less than the growth rate of the unstable whistler waves γ_w , which itself must be much less than the wave frequency ω_w of the unstable waves. Since the driving of the quasi-linear diffusion depends critically on the trapping effect, we require that ν_d is less than the trapping frequency $1/\tau_t$ of the bouncing electrons, where τ_t is the trapping time. The slowest process in our model is the ion-scale growth of the magnetic hole, estimated as the linear mirror-mode growth rate γ_m , which we thus set as the smallest characteristic frequency in our scenario. This timescale ordering of these processes is given by

$$\gamma_m \ll \nu_d \lesssim \frac{1}{\tau_t} \ll \gamma_w \ll \omega_w \lesssim \Omega_e. \quad (3)$$

3. Data Set

Only recently, direct in-situ measurements of the details of the electron behavior in magnetic holes on a short timescale

have become possible due to the unprecedented high time-resolution electron velocity distribution data from the MMS mission. We use data from the MMS mission when the spacecraft were in the Earth’s magnetosheath on 2017 January 25 from 00:25:40 UT to 00:26:15 UT. The magnetic-field data are provided by the fluxgate magnetometer (FGM; Russell et al. 2016). The high time-resolution electromagnetic-field data are provided by the search-coil magnetometer (SCM) and the electric double probes (EDP; Torbert et al. 2016). The particle velocity distribution data are retrieved by the fast plasma investigation (FPI; Pollock et al. 2016). We focus on the high time-resolution dynamics of wave–particle interactions and diffusion of the trapped electrons in the magnetic hole. All data used in this paper are high time-resolution burst mode data.

4. Results

4.1. Particle Trapping and Diffusion in the Magnetic Hole

Figures 2(a)–(j) show a magnetic hole crossing observed by MMS. Figures 2(a) and (b) show the ion density and magnetic-field strength observed by the four MMS, which were in a tetrahedral formation with a quality factor of 0.891 at the time of measurement. The four spacecraft observe almost identical profiles in the measured quantities due to the small spacecraft separation (≈ 10 km) compared to the size of the magnetic hole. We find a clear anticorrelation between the magnetic-field strength and the plasma density, which is a characteristic property of magnetic holes. The plasma density assumes its maximum when the magnetic field strength assumes its minimum at the center of the magnetic hole. Figure 2(c) shows the magnetic-field components observed by MMS1 in the Geocentric Solar Ecliptic coordinate system (GSE). The magnetic-field variations are dominated by the field’s z -component. Figures 2(f) and (g) show the differential energy fluxes of ions and electrons measured by FPI on board MMS1. The magnetosheath plasma is anisotropic in the magnetic hole and is composed of intense hot ions (few hundreds of eV) and cold electrons (few tens of eV). The electron energy exhibits a local enhancement inside the magnetic hole.

We calculate the linear growth rate of the mirror-mode instability using the New Hampshire Dispersion Relation Solver (NHDS; Verscharen & Chandran 2018) based on the observed plasma parameters. The average plasma parameters from 00:25:30 UT to 00:26:00 UT corresponding to about three wavelengths of the mirror mode are: the magnetic-field strength $B = 44.22$ nT, ion number density $n = 43.89$ cm $^{-3}$, proton perpendicular thermal speed $v_{\text{th,p}\perp} = 1.87 \times 10^2$ km s $^{-1}$, proton parallel thermal speed $v_{\text{th,p}\parallel} = 1.44 \times 10^2$ km s $^{-1}$, electron perpendicular thermal speed $v_{\text{th,e}\perp} = 3.03 \times 10^3$ km s $^{-1}$, electron parallel thermal speed $v_{\text{th,e}\parallel} = 2.89 \times 10^3$ km s $^{-1}$, and plasma bulk speed $v_{\text{sw}} = 123.89$ km s $^{-1}$. As shown in Figure 2(k), NHDS predicts that the plasma is unstable to the mirror-mode instability with a maximum growth rate of $\gamma_m \approx 0.0003$ Hz at a wavevector of about $k_m = 0.005$ km $^{-1}$, corresponding to a wavelength of about $\lambda_m = 2\pi/k_m = 1257$ km. The angle between the wavenumber at maximum growth and the magnetic field is 81° . Since the real frequency of mirror modes is zero (i.e., not propagating), this structure is convected by the plasma bulk flow. The NHDS results for all four MMS spacecraft measurements are almost identical because their separations are much smaller than the structure.

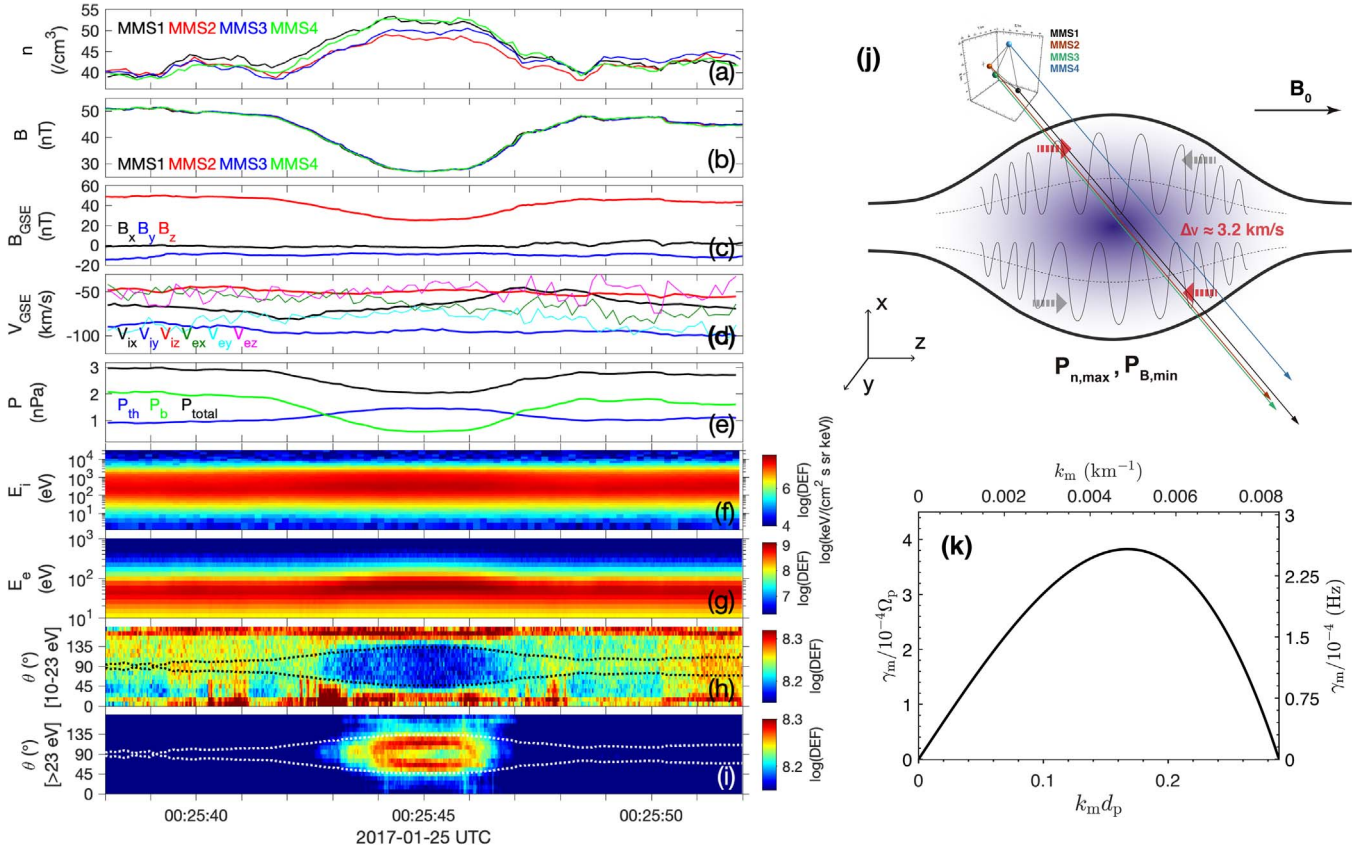


Figure 2. Magnetospheric Multiscale (MMS) mission observations of a magnetic hole on 2017 January 25 from 00:25:30 UT to 00:26:00 UT. (a) Ion number densities. (b) Magnetic-field strengths. (c) Magnetic-field components measured by MMS1 in GSE coordinates. (d) Velocity components of ions and electrons measured by MMS1 in GSE coordinates. (e) Ion thermal pressure, magnetic pressure, and the sum of thermal and magnetic pressures. (f) and (g) ion and electron differential energy flux spectrograms. (h) and (i) electron pitch-angle spectrograms of 10–23 eV and >23 eV electrons. The black/white dotted lines in (h) and (i) indicate the critical pitch angles according to Equation (1). (j) A sketch of the magnetic hole crossing by the MMS tetrahedron shown in GSE coordinates. (k) The growth rate of the mirror-mode instability calculated by NHDS using average parameters of the MMS1 measurements, where d_p is the proton inertial length and Ω_p is the proton gyrofrequency.

Figure 2(j) shows a sketch of the MMS trajectory during the magnetic hole crossing. The magnetic hole is elongated along the direction parallel to the magnetic field. The sampling direction relative to the magnetic-field direction of MMS largely depends on the angle between the plasma bulk flow and the background magnetic field (θ_{bv}), in this case $\theta_{bv} = 51^\circ$. Thus we approximate the convection time of a half-wavelength of the mirror-mode structure as

$$\tau_c = \frac{\lambda_m \sin 81^\circ}{2v_{sw} \sin \theta_{bv}} \approx 6.4 \text{ s}. \quad (4)$$

This value is in agreement with the duration of the magnetic hole in the MMS observation from 00:25:42 UT to 00:25:48 UT.

Figures 2(h) and (i) show the pitch-angle distribution functions of electrons with energies 10–23 eV and with energy greater than 23 eV. The black and the white dotted lines in Figures 2(h) and (i) represent the critical pitch angles θ_c and $180^\circ - \theta_c$ for particle trapping from Equation (1). Most of the electrons in these energy ranges are trapped in the magnetic hole (i.e., between both dotted lines). We approximate the typical electron trapping time as

$$\tau_t = \lambda_m / v_{th,||e} \approx 0.42 \text{ s}, \quad (5)$$

where $v_{th,||e}$ is the local thermal speed parallel to the magnetic field of the electrons at the center of the magnetic hole. The timescale of the electron bounce motion is much smaller than the convection

time ($\tau_t \ll \tau_c$). The depletion of electrons near 90° in Figures 2(h) and (i) is direct evidence for betatron cooling, which is referred to as donut-shaped pitch-angle distributions by recent in-situ observations (Soucek & Escoubet 2011; Ahmadi et al. 2018; Breuillard et al. 2018; Li et al. 2021). As the magnetic hole converges and the magnetic field decreases, betatron cooling reduces the perpendicular velocity of the trapped electrons. In our case, we find a strong depletion of 10–23 eV electrons inside the critical trapping angle in Figure 2(h).

Using the timing technique (Russell et al. 1983), we find that the magnetic hole converges at its inbound boundary with a velocity of about $[-0.25, 0.5, -3.25] \text{ km s}^{-1}$ in GSE coordinates. Due to the pressure gradient, this converging motion almost along the magnetic-field direction directly causes the Fermi acceleration of electrons. This is in agreement with the increase of electron energy in the energy spectrogram shown in Figure 2(g). The Fermi acceleration also leads to “X-shaped” leakage of >23 eV electrons to the loss cone as shown in Figure 2(i). All of these signatures are consistent with our predicted large-scale dynamics for a converging magnetic hole illustrated in panels (a) and (b) of Figure 1.

4.2. Resonant Instability of Counter-streaming Electron Beams

Figure 3 shows the contours of the electron VDF measured by FPI on board MMS1 near the center of the magnetic hole on 2017 January 25 between 00:25:44.38 UT and 00:26:44.80 UT.

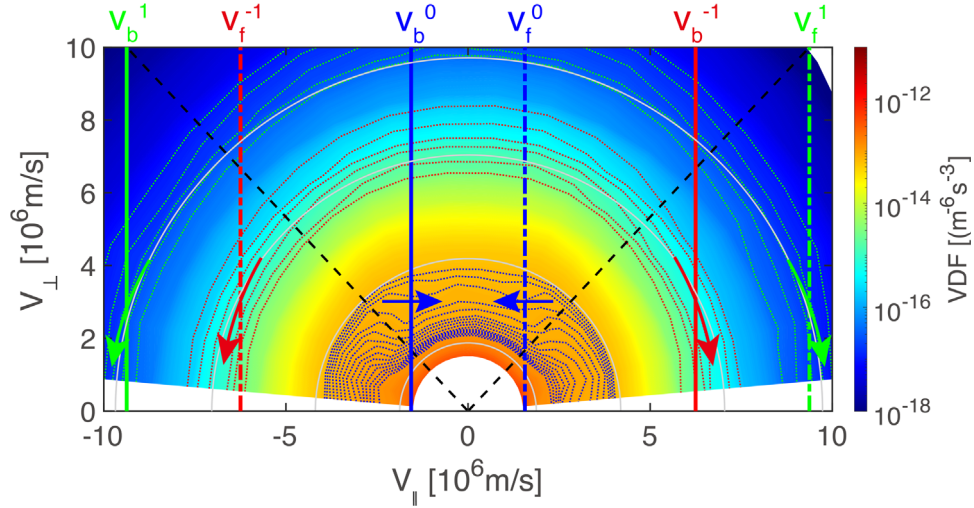


Figure 3. Averaged contour plot of the electron velocity distribution function (VDF) measured by MMS1 FPI in velocity space (v_{\parallel} , v_{\perp}) on 2017 January 25 from 00:25:44.38 UT to 00:25:44.80 UT. The blue solid and dashed lines denote the Landau resonance speeds with whistler waves calculated based on the local parameters. The red and green vertical lines denote the cyclotron resonance speeds with $n = -1$ and $n = 1$ in Equation (6). Dashed and solid line styles represent the resonance speed for the forward-propagating and backward-propagating waves. The black dashed lines represent the critical pitch-angle θ_c according to Equation (1). The colored arrows represent the quasi-linear diffusion trajectories of resonant interactions. The gray semicircles represent constant kinetic energy (i.e., $v_{\perp}^2 + v_{\parallel}^2 = \text{constant}$). The colored contour lines are highlighted to show the local gradients of the VDF. VDF values smaller or greater than the color bar range are not shown here.

The VDFs from all four MMS spacecraft are nearly identical. Errors from photoelectrons and secondary electrons are corrected in the VDFs (see Appendix C). We plot the contours of $f_e(v_{\parallel}, v_{\perp})$ in a layout similar to Figure 1(b). The black dashed lines denote the critical pitch-angles θ_c and $180^\circ - \theta_c$ according to Equation (1). The blue vertical lines show the Landau resonance speeds of forward-propagating (dashed) whistler waves with phase speed v_f^0 and backward-propagating (solid) whistler waves with phase speed v_b^0 for which the integer n in Equation (2) is equal to zero. The red vertical line represents the cyclotron resonance speeds for $n = -1$ in Equation (2) for forward-propagating (dashed) and backward-propagating (solid) whistler waves. The green lines mark the same for $n = +1$ in Equation (2) for forward-propagating (dashed) and backward-propagating (solid) whistler waves.

The electron VDF is non-Maxwellian and has two significant enhancements near $v_{\parallel} \approx \pm 1.5 \times 10^3 \text{ km s}^{-1}$, corresponding to a pair of counterstreaming electron beams with energies between 10–23 eV. This pair of electron beams is partially located just outside the critical trapping pitch angle (i.e., inside the loss cone), consistent with our prediction shown in Figure 1(b).

We calculate the Landau resonance speed of forward-propagating (backward-propagating) whistler waves $v_f^0 = 1.43 \times 10^3$ ($v_b^0 = -1.43 \times 10^3$) km s^{-1} by inserting $n = 0$ to

$$v_{b/f}^n = \left(\frac{B^2}{\mu_0 m_e n_e \omega_w \cos^2 \theta_k} \left(\cos \theta_k - \frac{\omega_w}{\Omega_e} \right) \left(n + \frac{\omega_w}{\Omega_e} \right)^2 \right)^{\frac{1}{2}}, \quad (6)$$

which is a quasi-linear approximation based on the cold-plasma dispersion relation (Lengyel-Frey et al. 1994), where μ_0 is the vacuum permeability. We use a wave angle $\theta_k = 10^\circ$ and a ratio between the whistler waves and electron gyrofrequency of $\omega_w/\Omega_e = 0.3$ since this is close to the frequency of whistler waves in our observation (see Section 4.3 for more details).

We find that $\partial f_e / \partial v_{\parallel} > 0$ at $v_f^0 = 1.43 \times 10^3 \text{ km s}^{-1}$ and $\partial f_e / \partial v_{\parallel} < 0$ at $v_b^0 = -1.43 \times 10^3 \text{ km s}^{-1}$, meaning that Landau resonance with the electric-field component E_{\parallel} parallel to the background magnetic field leads to an instability of the resonant waves. If the whistler waves are not exactly parallel, they have a sufficient amplitude in E_{\parallel} and can thus participate in Landau-resonant wave–particle interactions. This result strongly suggests that the counter-streaming electron beams are the local driver for the whistler-wave generation in the magnetic hole. During the whistler-wave generation, the unstable electron VDF diffuses as shown in panel (c) of Figure 1 of our conceptual model. Like in our Figure 1(c), we use the blue arrows to show the quasi-linear diffusion trajectories of the resonant wave–particle interaction in Figure 3.

Depending on the local gradient of the electron VDF at the cyclotron resonance speeds, cyclotron-resonant interactions also contribute to the growth/damping of the whistler waves. We use the red and green arrows in Figure 3 to show possible diffusion paths of cyclotron-resonant electrons in velocity space. In our particular example, the cyclotron-resonant electrons with $n = -1$ decrease in their kinetic energy if the diffusive particle flux in velocity space is directed along the green arrows shown in Figure 3. This cyclotron-resonant interaction contributes to the growth of the resonant whistler waves. In the case of forward-propagating whistler waves with $\omega_w/k_{\parallel} > 0$, the most-efficient available cyclotron resonance for electron–wave interactions is the resonance with $n = -1$. In the case of backward-propagating whistler waves with $\omega_w/k_{\parallel} < 0$, it is the resonance with $n = 1$. However, in the case of the resonance with $n = 1$, the direction of the diffusive particle flux is toward greater ($v_{\perp}^2 + v_{\parallel}^2$) due to the gradients of the electron VDF at the resonance speed, which thus corresponds to a contribution to the damping of the resonant whistler waves. The overall instability of the whistler waves is the result of contributions from resonances with all accessible n .

Table 1
The Fitting Parameters of Our VDF Data Shown in Figure 3 on 2017 January 25 from 00:25:44.38 UT to 00:26:44.80 UT

| | n_j (m^{-3}) | $v_{\text{th}\perp j}$ (m/s) | $v_{\text{th}\parallel j}$ (m/s) | $u_{\parallel j}$ (m/s) | $u_{\perp j}$ (m/s) |
|--------|--------------------------------------|------------------------------------|--|-------------------------|---------------------|
| Beam 1 | 2.18×10^6 | 2.77×10^6 | 1.17×10^6 | 2.99×10^6 | 3.99×10^5 |
| Beam 2 | 4.11×10^6 | 3.27×10^6 | 1.05×10^6 | -2.86×10^6 | -6.35×10^5 |
| Core | 1.74×10^7 | 1.11×10^6 | 1.16×10^6 | 8.71×10^3 | |
| | A ($\text{m}^{-6}\text{s}^{-3}$) | $v_{\text{th}\perp\text{M}}$ (m/s) | $v_{\text{th}\parallel\text{M}}$ (m/s) | | |
| Moyal | 0.82×10^{-13} | 4.52×10^6 | 3.91×10^6 | | |

4.3. Properties of the Unstable Whistler Waves: Theory and Observations

We mathematically evaluate the consequence of the large-scale convergence: the stability of the observed electron VDFs in the magnetic hole, with the Arbitrary Linear Plasma Solver (ALPS) code (Verscharen et al. 2018). We model the electron VDF by using a four-component VDF model, which has two drifting electron beams, one Maxwellian core, and one modified Moyal distribution to model the observed flat-top distribution (see Appendix B for more details). Different from traditional Maxwellian plasma dispersion solvers, ALPS allows us to include the non-Maxwellian Moyal component. We implement a fitting technique for the electron VDF data around the center of the whistler-wave emission on 2017 January 25 from 00:25:44.38 UT to 00:26:44.80 UT. The fit parameters for the electron VDF shown in Figure 3 are listed in Table 1. The electron plasma frequency is about $13\Omega_e$ (i.e., 6.33×10^4 Hz).

The growth rate and real frequency of the unstable whistler-mode predicted by our ALPS calculations are shown in Figures 4(j) and (k). With a wave angle of $\theta_k = 10^\circ$, the whistler wave has a growth rate of $\gamma_w = 27$ Hz and a real frequency of $f_w \approx 203$ Hz at a wavevector of $k_w = 0.88 \text{ km}^{-1}$. We find the corresponding phase speed of $v_w = 2\pi f_w / k_w \approx 1.45 \times 10^3 \text{ km s}^{-1}$.

We show the observed whistler waves with the help of high-cadence data of electric and magnetic fields measured by the SCM and EDP instruments on board MMS1. We use the electric-field fluctuations in a field-aligned coordinate system based on the average background magnetic field. Figures 4(a)–(c) show that the electric-field fluctuations parallel to the magnetic field E_{\parallel} have a significant enhancement near the magnetic field minimum at the center of the magnetic hole. The parallel electric-field enhancement in the gray-shaded region coincides with the VDF shown in Figure 3.

Consistently with our multiscale ordering and the required properties of resonant whistler waves, we find that slightly oblique whistler waves exist near and at the center of the magnetic hole. Figures 4(d)–(i) show the polarization properties of the detected electromagnetic-field fluctuations. We use the singular value decomposition method to calculate the power spectral densities of the perpendicular magnetic-field fluctuations, the parallel electric-field fluctuations, and the polarization properties of the wave fields, such as the ellipticity, the wave angle θ_k , the phase speed, and the Poynting flux (Santolík et al. 2003).

As shown in Figures 4(d)–(e), we find significant enhancements of the perpendicular magnetic field and the parallel electric-field fluctuations at about 202 Hz (i.e., about $0.26 \Omega_e$) near the center of the magnetic hole on 2017 January 25 between 00:25:44.48 UT and 00:26:44.54 UT. Within this interval, the ellipticity of the wave and the degree of

polarization is close to unity, suggesting a slightly oblique right-hand polarized wave. The phase speed averaged at the frequency of 202 Hz during this interval is about $1.58 \times 10^3 \text{ km s}^{-1}$. The wave propagates with an average angle of $\theta_k \approx 9^\circ$ with respect to the direction parallel or antiparallel to the magnetic field. The whistler waves propagate away from the source and predominantly along the field direction. Since the counter-streaming electron beams are not exactly symmetric, we observe an unbalanced Poynting flux in the waves. These observations are in good agreement with the predictions of our ALPS calculations.

We estimate the diffusion rate ν_d based on the quasi-linear approximation as

$$\nu_d \approx \frac{c^2 \Omega_e^2}{2B_0^2} \frac{v_{\text{sw}} k_w^3}{\omega_w^3} \hat{E}_{\parallel}^2(\omega_w) \cos \theta_{\text{bv}} = 0.25 \text{ Hz}, \quad (7)$$

where c is the speed of light and \hat{E}_{\parallel}^2 is the power spectral density of the component of electric-field fluctuations parallel to the magnetic field at a frequency of 202 Hz (see Appendix A for more details). As required in Equation (2), the diffusion rate lies between the fast whistler-wave growth ($\gamma_w \approx 27$ Hz) and the slow mirror instability growth ($\gamma_m \approx 0.0003$ Hz). The wavelength of the whistler wave is about $\lambda_w = 2\pi/k_w \approx 7$ km, which is equivalent to about $10\rho_e$. We note this characteristic length is much smaller than the length scale of the magnetic hole. This scale ordering is consistent with our scenario that the whistler waves are locally generated and diffuse electrons via resonant interactions at the local gradients of the VDF shown in Figures 1 and 3.

5. Discussion and Conclusions

We show clear in-situ evidence for resonant wave–particle interaction between electrons and slightly oblique whistler waves in a converging magnetic hole in the Earth’s magnetosheath. We propose a conceptual model and a consistent ordering for the multiscale particle dynamics in such a structure. In this model, a converging magnetic hole generates whistler waves through the interplay between Fermi acceleration, betatron cooling, and resonant wave–particle interactions.

We test this idea with MMS observations of a magnetic hole that converges with a velocity of $[-0.25, 0.5, -3.25] \text{ km s}^{-1}$ mostly in the direction of the background magnetic field. As proposed in our model, a pair of counterstreaming electron beams is produced.

We observe and explain the local generation of whistler waves at the magnetic hole center by a combination of Landau-resonant and cyclotron-resonant wave–particle interactions. The Landau-resonant interaction is of particular interest for our

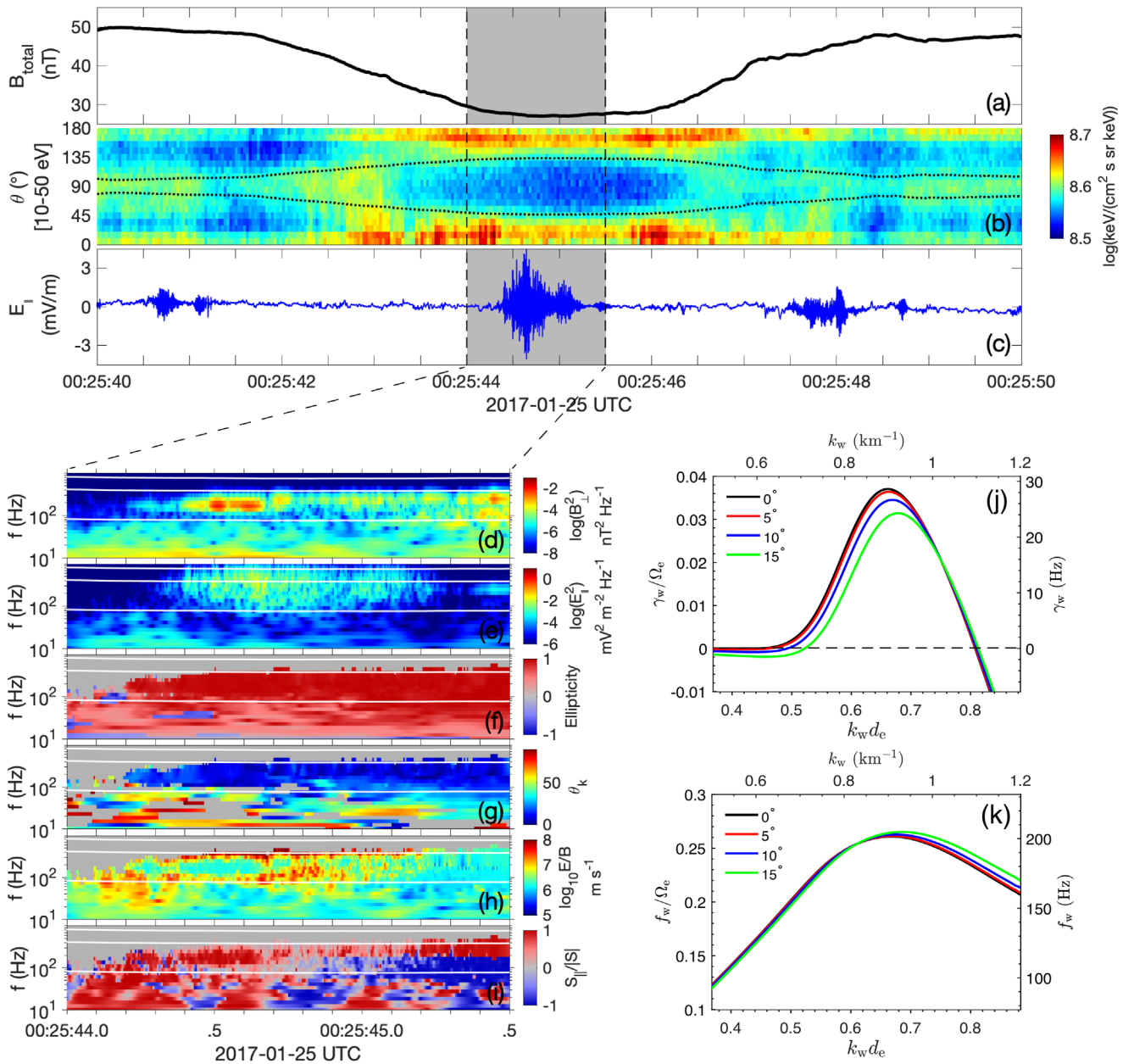


Figure 4. Polarization magnetic analysis and numerical prediction of the unstable whistler waves from MMS1. (a) The magnetic-field strength. (b) Pitch-angle distribution of electrons from FPI with energy within 10–50 eV. (c) The parallel electric field from EDP. (d) The power spectral density of the magnetic-field fluctuations perpendicular to the background from SCM. (e) The power spectral density of the electric-field fluctuations parallel to the background from EDP. (f) The ellipticity. (g) The wave angle θ_k . (h) The phase speed. (i) The Poynting flux. The three white solid lines in (d)–(i) represent frequencies corresponding to $0.1\Omega_e$, $0.5\Omega_e$, and Ω_e . (j) and (k) our model predictions of the growth rate and the frequency of unstable whistler-mode with different wave angles calculated by ALPS.

understanding of the evolution of the magnetic hole. It fills the velocity space between the electron beams and thus effectively smooths out the nonthermal features created by Fermi acceleration and betatron cooling.

The studied magnetic hole fulfills the ordering of scales from Equation (3): (1) The maximum growth rate of the mirror-mode instability is $\gamma_m \approx 0.0003$ Hz at a wavelength of ≈ 1257 km. (2) The estimated quasi-linear diffusion rate for the Landau-resonant wave-particle interaction of electrons is 0.25 Hz. (3) The typical trapping frequency of electrons is 2.38 Hz. (4) The growth rate of the unstable whistler waves is 30 Hz. (5) The frequency of the unstable whistler waves is about 202 Hz. In this ordering, the Landau-resonant wave-particle interaction secularly transfers the kinetic energy of electrons to the unstable whistler waves on a

timescale greater than the typical time of the electron bounce motion in the magnetic hole structure.

Our study develops and confirms a consistent understanding of the evolution of converging magnetic holes. Magnetic holes are an important type of coherent structure in space plasmas that evolve through a multiscale process that couples the kinetic dynamics of particle diffusion and energy transfer at electron scales. As a remarkable signature of these converging magnetic holes, we find that whistler waves are an important feature of local energy emission from the kinetic energy of resonant electrons. We note that the saturation and nonlinear development of the mirror-mode instability play a nontrivial role in the particle diffusion in magnetic holes (e.g., Kivelson & Southwood 1996; Kuznetsov et al. 2007). As a type of quasi-steady plasma structure, magnetic

holes experience different stages of their evolution, in some of which electron-scale waves are present or absent (e.g., Ahmadi et al. 2018; Huang et al. 2019). Figure 4(e) shows the existence of electrostatic fluctuations above the frequency of our whistler waves. Multiple forms of kinetic waves such as electrostatic solitary waves and electron cyclotron waves have been observed in magnetic holes (e.g., Yao et al. 2019). However, these additional wave–particle mechanisms associated with magnetic holes remain beyond the scope of our current analysis.

Building on our model and observations, it would be worthwhile to undertake a full numerical evaluation of the adiabatic effects and the resonant evolution in a quasi-linear framework. This would further improve our understanding of the multiscale particle dynamics in coherent structures.

We thank the MMS team for data. All of the data used in this paper are accessible at the MMS Science Data Center (<https://lasp.colorado.edu/mms/sdc/public>). The code for data and polarization analysis is publicly available via <https://github.com/irfu>. More description on the Arbitrary Linear Plasma Solver (ALPS) and the New Hampshire Dispersion Relation Solver (NHDS) can be found via <http://www.alps.space> and <https://github.com/danielver02/NHDS>. W.J. thanks Dr. Wenya Li, Dr. Bingbing Tang, Dr. Seong-Yeop Jeong, Dr. Yong Ren, Dr. Chen Zeng, Chuanhui Gao, and Xingyu Zhu for helpful discussions and suggestions. This work is supported by NNSFC grants (42022032, 41874203, 42188101), project of Civil Aerospace “13th Five Year Plan” Preliminary Research in Space Science (D020301, D030202), Strategic Priority Research Program of CAS (grant No. XDA17010301), and Key Research Program of Frontier Sciences CAS (grant No. QYZDJ-SSW-JSC028). W.J. is supported by the CAS joint Ph.D. training program during his stay at UCL’s MSSSL. D.V. is supported by the STFC Ernest Rutherford Fellowship ST/P003826/1 and STFC Consolidated grants ST/S000240/1 and ST/W001004/1. H.L. is supported by International Partnership Program of CAS (grant No. 183311KYBS20200017) and in part by the Specialized Research Fund for State Key Laboratories of China. K.G.K. is supported by grant DE-SC0020132. This work was discussed at the “Joint Electron Project” (JEP) at MSSSL.

Appendix A

Estimate for the Quasi-linear Diffusion Rate

In quasi-linear theory, the Landau-resonant wave–particle interaction between electrons and slightly oblique whistler waves leads to a slow (compared to the wave period) time evolution of the VDF according to Kennel & Engelmann (1966) and Marsch (2006):

$$\frac{\partial f_e}{\partial t} \approx \frac{e^2}{8\pi^2 m_e^2 V} \int \left(\frac{k_{\parallel}}{\omega_w} \right)^2 \tilde{G} \frac{1}{|v_{\parallel}|} \times \delta(\omega_w - k_{\parallel} v_{\parallel}) |\psi|^2 \tilde{G} f_e d^3k, \quad (\text{A1})$$

where V is the volume in which the wave amplitude is effective to cause wave–particle interactions,

$$\tilde{G} \approx \frac{k_{\parallel} v_{\perp}}{\omega_w} \frac{\partial}{\partial v_{\parallel}}, \quad (\text{A2})$$

$$\psi \approx \frac{v_{\parallel}}{v_{\perp}} \tilde{E}_z, \quad (\text{A3})$$

and \tilde{E}_z is the Fourier amplitude of the parallel component of the electric-field fluctuations. Resolving the δ function in Equation (A1), we obtain the simplified quasi-linear diffusion equation:

$$\frac{\partial f_e}{\partial t} \approx \frac{e^2}{8\pi^2 m_e^2 V} \frac{\partial}{\partial v_{\parallel}} \times \int \frac{1}{|v_{\parallel}|} \left| \tilde{E}_z \left(k_{\parallel} = \frac{\omega_w}{v_{\parallel}} \right) \right|^2 \frac{\partial f_e}{\partial v_{\parallel}} dk_x dk_y, \quad (\text{A4})$$

where k_x and k_y are perpendicular components of the wavevector k . Assuming that the electric-field fluctuations have a significant effect on a finite range of k_{\parallel} values with width Δk_{\parallel} , we find

$$\int |\tilde{E}_z|^2 dk_x dk_y = \frac{8\pi^3 V}{\Delta k_{\parallel}} \delta E^2, \quad (\text{A5})$$

where Δk_{\parallel} is a finite parallel wavenumber range in which the wave power δE^2 is distributed. We approximate δE^2 of the observed whistler waves by using the power spectral density of the electric-field fluctuations $\hat{E}_{\parallel}^2(\omega)$ in a narrow range of frequency $\Delta\omega_w$ in the spacecraft frame according to

$$\delta E^2 = \int \hat{E}_{\parallel}^2(\omega) d\omega \approx \hat{E}_{\parallel}^2(\omega_w) \Delta\omega_w. \quad (\text{A6})$$

We then use Taylor’s hypothesis (Taylor 1938)

$$2\pi\Delta\omega \approx v_{sw} \cos\theta_{bv} \Delta k_{\parallel}, \quad (\text{A7})$$

to express

$$\int |\tilde{E}_z|^2 dk_x dk_y = 4\pi^2 V v_{sw} \hat{E}_{\parallel}^2(\omega_w) \cos\theta_{bv}. \quad (\text{A8})$$

This allows us to estimate the effect of the quasi-linear diffusion as

$$\frac{\partial f_e}{\partial t} \approx \frac{\partial^2}{\partial v_{\parallel}^2} (\tilde{D} f_e), \quad (\text{A9})$$

where

$$\tilde{D} = \frac{\omega_w^2}{k_w^2} \nu_d \quad (\text{A10})$$

is the effective diffusion coefficient and

$$\nu_d \approx \frac{c^2 \Omega_e^2 v_{sw} k_w^3}{2B_0^2 \omega_w^3} \hat{E}_{\parallel}^2(\omega_w) \cos\theta_{bv} \quad (\text{A11})$$

is the estimated diffusion rate. Based on the solutions ω_w and k_w from our linear theory results and with $\hat{E}_{\parallel}^2 \approx 6 \times 10^{-4} \text{ mV}^2 \text{ m}^{-2} \text{ Hz}^{-1}$ from our observations at 202 Hz, we obtain the diffusion rate of $\nu_d \approx 0.25 \text{ Hz}$.

Appendix B

VDF Model and the Arbitrary Linear Plasma Solver

The measured distribution of the trapped particles in magnetic holes deviates from the equilibrium Maxwellian distribution, especially due to the presence of the discussed electron beams and the flat-top part of the distribution, which we model with a bi-Moyal distribution. The bi-Moyal

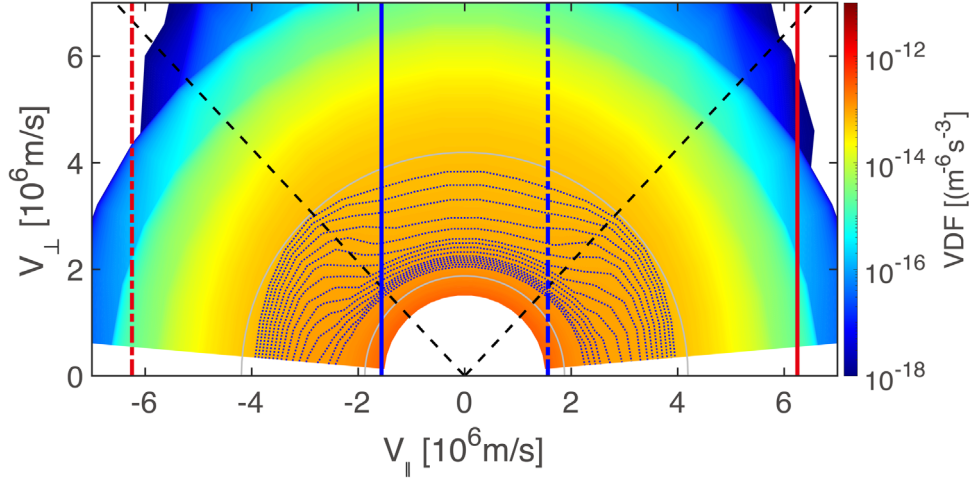


Figure 5. Contour plot of our velocity distribution function (VDF) model according to Equation (B1) based on the averaged electron VDF data on 2017 January 25 from 00:25:44.38 to 00:26:44.80 UT observed by MMS1. The format is the same as Figure 3.

distribution is a two-dimensional extension of the modified Moyal distribution (Klein & Chandran 2016).

To solve the full hot-plasma dispersion relation, we implement a VDF fitting model as input to our ALPS solver. Our VDF model is a combination of three bi-Maxwellian distributions (two beams f_b and one core f_c) and one bi-Moyal distribution f_M :

$$f_e = f_c + f_b + f_M, \quad (\text{B1})$$

where

$$f_b(v_{\parallel}, v_{\perp}) = \sum_{j=1}^2 \frac{n_j}{\pi^{3/2} v_{\text{th}\perp j}^2 v_{\text{th}\parallel j}} \times \exp\left(-\frac{(v_{\perp} - u_{\perp j})^2}{v_{\text{th}\perp j}^2} - \frac{(v_{\parallel} - u_{\parallel j})^2}{v_{\text{th}\parallel j}^2}\right), \quad (\text{B2})$$

$$f_c(v_{\parallel}, v_{\perp}) = \frac{n_3}{\pi^{3/2} v_{\text{th}\perp 3}^2 v_{\text{th}\parallel 3}} \times \exp\left(-\frac{v_{\perp}^2}{v_{\text{th}\perp 3}^2} - \frac{(v_{\parallel} - u_{\parallel 3})^2}{v_{\text{th}\parallel 3}^2}\right), \quad (\text{B3})$$

$$f_M(v_{\parallel}, v_{\perp}) = A \exp\left(\frac{1}{2} \left[\frac{v_{\perp}^2}{v_{\text{th}\perp M}^2} + \frac{v_{\parallel}^2}{v_{\text{th}\parallel M}^2} - \exp\left(\frac{v_{\perp}^2}{v_{\text{th}\perp M}^2} + \frac{v_{\parallel}^2}{v_{\text{th}\parallel M}^2}\right) \right]\right), \quad (\text{B4})$$

n_j , $v_{\text{th}\perp j}$, $v_{\text{th}\parallel j}$, $v_{\text{th}\perp M}$, $v_{\text{th}\parallel M}$, $u_{\perp j}$, $u_{\parallel j}$, and A are fit parameters. Using the Levenberg–Marquardt fitting technique (Press et al. 1996),

we obtain model parameters for the total electron VDF by minimizing the residual error.

We show the obtained parameters for our VDF model in Table 1 and the corresponding contour plot of the VDF model in Figure 5. The minimized sum of squared residuals is 0.14 on a logarithmic scale, indicating a good approximation to the real MMS VDF data. In fact, by comparing to previous models with only bi-Maxwellian components (e.g., Huang et al. 2020; Zhang et al. 2021), we find that our model is a simple and realistic description.

Appendix C

Impact of Photoelectrons and Secondary Electrons

Photoelectrons and secondary electrons are the main sources of error in the measurement of the electron velocity distribution function. Electrons are produced when EUV photons strike a spacecraft surface or an instrument, resulting in both internal and external errors in electron measurements. The finite spacecraft potential ϕ accelerates low-energy electrons and modifies the measurements in the energy range $\lesssim |e\phi|$. MMS has a spacecraft potential controller (ASPOC) that can actively reduce the absolute spacecraft potential and consequently the energy of spacecraft photoelectrons.

Figure 6(a) shows the spacecraft potential, which is ≈ 2.18 V during our measurement interval, suggesting that the error from spacecraft photoelectrons is negligible in our study.

When the instrument faces the Sun, secondary electrons are produced inside the instrument and independent of spacecraft potential. Figures 6(b) and (c) show the electron VDF without correction and the VDF of secondary electrons being corrected. We apply this correction throughout our analysis. More details about the correction are given at <https://lasp.colorado.edu/galaxy/display/MFDPG/DES+Photoelectrons+-+further+details>.

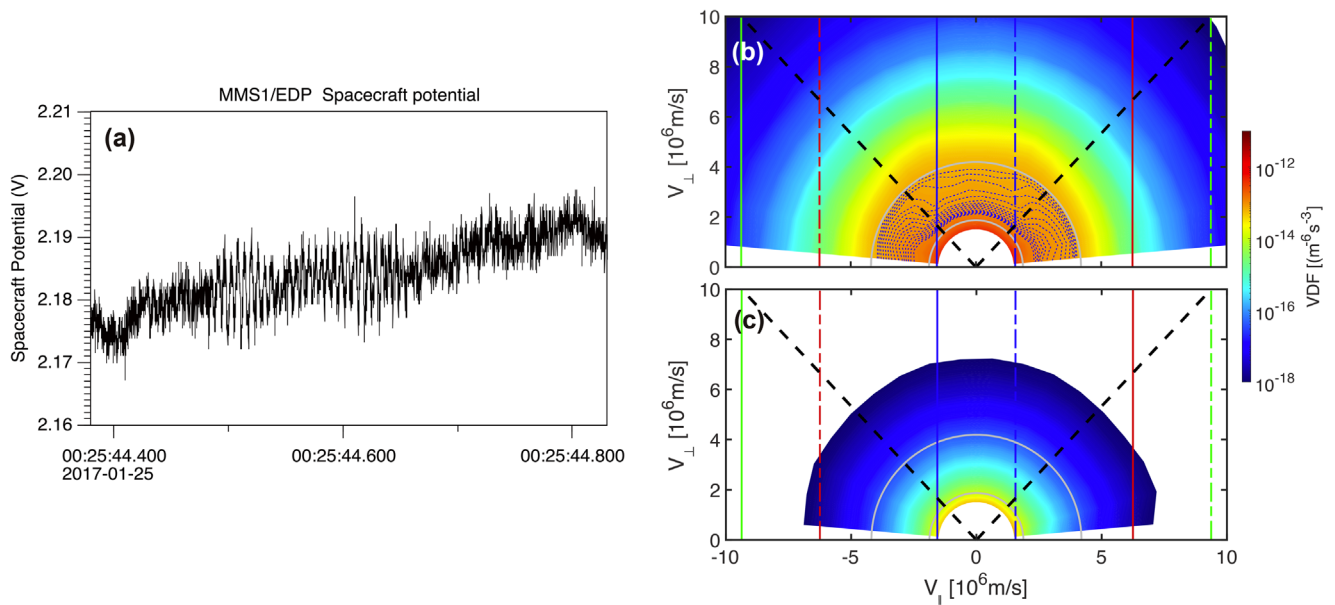


Figure 6. Errors of electron velocity distribution function. (a) MMS1 electric double probes (EDP) spacecraft potential. (b) The contour plot of the electron VDF without secondary electrons removed. (c) The contour plot of the secondary electron VDF. The VDF time intervals selected in (b) and (c) are the same as in Figure 3.

ORCID iDs

Wence Jiang <https://orcid.org/0000-0001-7431-5759>
 Daniel Verscharen <https://orcid.org/0000-0002-0497-1096>
 Hui Li <https://orcid.org/0000-0002-4839-4614>
 Chi Wang <https://orcid.org/0000-0001-6991-9398>
 Kristopher G. Klein <https://orcid.org/0000-0001-6038-1923>

References

- Ahmadi, N., Wilder, F. D., Ergun, R. E., et al. 2018, *JGRA*, **123**, 6383
 Alexandrova, O., Chen, C. H. K., Sorriso-Valvo, L., Horbury, T. S., & Bale, S. D. 2013, *SSRv*, **178**, 101
 Baumgärtel, K. 1999, *JGRA*, **104**, 28295
 Behar, E., Sahraoui, F., & Berčić, L. 2020, *JGRA*, **125**, e28040
 Breuillard, H., Le Contel, O., Chust, T., et al. 2018, *JGRA*, **123**, 93
 Burlaga, L. F., Ness, N. F., & Acuña, M. H. 2006, *GeoRL*, **33**, L21106
 Cattaneo, M. B. B., Basile, C., Moreno, G., & Richardson, J. D. 1998, *JGRA*, **103**, 11961
 Chandrasekhar, S., Kaufman, A. M., & Watson, K. M. 1958, *RSPSA*, **245**, 435
 Chisham, G., Burgess, D., Schwartz, S. J., & Dunlop, M. W. 1998, *JGRA*, **103**, 26765
 Fazakerley, A., Coates, A., & Dunlop, M. 1995, *AdSpR*, **15**, 349
 Fazakerley, A., & Southwood, D. 1994, *AdSpR*, **14**, 65
 Gary, S. P. 1993, *Theory of Space Plasma Microinstabilities*, Cambridge Atmospheric and Space Science Series (Cambridge: Cambridge Univ. Press)
 Hasegawa, A. 1969, *PhFI*, **12**, 2642
 Haynes, C. T., Burgess, D., Camporeale, E., & Sundberg, T. 2015, *PhPI*, **22**, 012309
 Huang, S. Y., He, L. H., Yuan, Z. G., et al. 2019, *ApJ*, **875**, 113
 Huang, S. Y., Xu, S. B., He, L. H., et al. 2020, *GeoRL*, **47**, e87515
 Jeong, S.-Y., Verscharen, D., Wicks, R. T., & Fazakerley, A. N. 2020, *ApJ*, **902**, 128
 Karimabadi, H., Roytershteyn, V., Vu, H. X., et al. 2014, *PhPI*, **21**, 062308
 Kaufmann, R. L., Horng, J.-T., & Wolfe, A. 1970, *JGR*, **75**, 4666
 Kennel, C. F., & Engelmann, F. 1966, *PhFI*, **9**, 2377
 Kitamura, N., Omura, Y., Nakamura, S., et al. 2020, *JGRA*, **125**, e27488
 Kivelson, M. G., & Southwood, D. J. 1996, *JGRA*, **101**, 17365
 Klein, K. G., & Chandran, B. D. G. 2016, *ApJ*, **820**, 47
 Kunz, M. W., Schekochihin, A. A., & Stone, J. M. 2014, *PhRvL*, **112**, 205003
 Kuznetsov, E. A., Passot, T., & Sulem, P. L. 2007, *PhRvL*, **98**, 235003
 Lengyel-Frey, D., Farrell, W. M., Stone, R. G., Balogh, A., & Forsyth, R. 1994, *JGR*, **99**, 13325
 Li, J.-H., Zhou, X.-Z., Zong, Q.-G., et al. 2021, *GeoRL*, **48**, e91613
 Li, Z.-Y., Sun, W.-J., Wang, X.-G., et al. 2016, *JGRA*, **121**, 4180
 Liu, Y. Y., Fu, H. S., Zong, Q. G., et al. 2020, *GeoRL*, **47**, e88374
 Marsch, E. 2006, *LRSP*, **3**, 1
 Pantellini, F., Burgess, D., & Schwartz, S. 1995, *AdSpR*, **15**, 341
 Plaschke, F., Hietala, H., Archer, M., et al. 2018, *SSRv*, **214**, 81
 Pollock, C., Moore, T., Jacques, A., et al. 2016, *SSRv*, **199**, 331
 Press, W. H., Teukolsky, S. A., Vetterling, W. T., & Flannery, B. P. 1996, *Numerical Recipes in Fortran 90: Numerical recipes in Fortran 77V. 2. Numerical recipes in Fortran 90* (Cambridge: Cambridge Univ. Press), 90
 Ren, Y., Dai, L., Li, W., et al. 2019, *GeoRL*, **46**, 5045
 Retinò, A., Sundkvist, D., Vaivads, A., et al. 2007, *NatPh*, **3**, 235
 Rowlands, J., Shapiro, V. D., & Shevchenko, V. I. 1966, *JETP*, **23**, 651
 Russell, C. T., Anderson, B. J., Baumjohann, W., et al. 2016, *SSRv*, **199**, 189
 Russell, C. T., Mellott, M. M., Smith, E. J., & King, J. H. 1983, *JGR*, **88**, 4739
 Russell, C. T., Riedler, W., Schwingenschuh, K., & Yeroshenko, Y. 1987, *GeoRL*, **14**, 644
 Sahraoui, F., Belmont, G., Rezeau, L., et al. 2006, *PhRvL*, **96**, 075002
 Santolík, O., Parrot, M., & Lefeuvre, F. 2003, *RaSc*, **38**, 1010
 Schekochihin, A. A., Cowley, S. C., Dorland, W., et al. 2009, *ApJS*, **182**, 310
 Schwartz, S. J., Burgess, D., & Moses, J. J. 1996, *AnGeo*, **14**, 1134
 Shapiro, V., & Shevchenko, V. 1962, *Sov. Phys. JETP*, **15**, 1053
 Soucek, J., & Escoubet, C. P. 2011, *AnGeo*, **29**, 1049
 Soucek, J., Lucek, E., & Dandouras, I. 2008, *JGRA*, **113**, A04203
 Southwood, D. J., & Kivelson, M. G. 1993, *JGR*, **98**, 9181
 Taylor, G. I. 1938, *RSPSA*, **164**, 476
 Torbert, R. B., Russell, C. T., Magnes, W., et al. 2016, *SSRv*, **199**, 105
 Tsurutani, B. T., Dasgupta, B., Galvan, C., et al. 2002, *GeoRL*, **29**, 86
 Tsurutani, B. T., Lakhina, G. S., Verkhoglyadova, O. P., et al. 2011, *JGRA*, **116**, A02103
 Tsurutani, B. T., Smith, E. J., Anderson, R. R., et al. 1982, *JGR*, **87**, 6060
 Verscharen, D., & Chandran, B. D. G. 2018, *RNAAS*, **2**, 13
 Verscharen, D., Chandran, B. D. G., Jeong, S.-Y., et al. 2019a, *ApJ*, **886**, 136
 Verscharen, D., Klein, K. G., Chandran, B. D. G., et al. 2018, *JPIPh*, **84**, 905840403
 Verscharen, D., Klein, K. G., & Maruca, B. A. 2019b, *LRSP*, **16**, 5
 Yao, S. T., Hamrin, M., Shi, Q. Q., et al. 2020, *JGRA*, **125**, e26736
 Yao, S. T., Shi, Q. Q., Yao, Z. H., et al. 2019, *GeoRL*, **46**, 523
 Zhang, H., Zhong, Z., Tang, R., et al. 2021, *GeoRL*, **48**, e96056
 Zhang, Y., Matsumoto, H., & Kojima, H. 1998, *JGRA*, **103**, 4615
 Zhima, Z., Cao, J., Fu, H., et al. 2015, *JGRA*, **120**, 2469